

Informing the improvement of forest products durability using small angle neutron scattering

Nayomi Z. Plaza · Sai Venkatesh Pingali · Shuo Qian · William T. Heller · Joseph E. Jakes

Received: 23 November 2015 / Accepted: 4 April 2016 / Published online: 15 April 2016
© Springer Science+Business Media Dordrecht (outside the USA) 2016

Abstract A better understanding of how wood nanostructure swells with moisture is needed to accelerate the development of forest products with enhanced moisture durability. Despite its suitability to study nanostructures, small angle neutron scattering (SANS) remains an underutilized tool in forest products research. Nanoscale moisture-induced structural changes in intact and partially cut wood cell walls were investigated using SANS and a custom-built relative humidity (RH) chamber. SANS from intact wood sections cut from each primary wood orientation showed that although wood scattered anisotropically across 1.3–600 nm length scales, measurement of elementary fibril spacing and low- q surface scattering were independent of orientation. Water sorption

caused spacing between elementary fibrils to increase with RH, and this swelling accounted for over half the transverse swelling in S2 secondary wood cell walls. Elementary fibril spacing in longitudinally cut wood cells, which were designed to mimic cells near wood-adhesive bondlines, was greater than the spacing in intact cells above 90 % RH. This suggested that some cell wall hoop constraint from the S1 and S3 cell wall layers on the S2 layer was released by cutting the cells. Furthermore, increased spacing between elementary fibrils may also create diffusion channels that are hypothesized to be responsible for the onset of fungal decay in wood. Protocols were established to use SANS in future research to study adhesives and protection treatments to improve moisture durability in forest products.

Keywords Small angle neutron scattering · Cellulose elementary fibrils · Moisture content · Wood

N. Z. Plaza
Materials Science Program, University of Wisconsin-Madison, 1509 University Avenue, Madison, WI 53706, USA

N. Z. Plaza · J. E. Jakes (✉)
Forest Biopolymer Science and Engineering, U.S. Forest Service, Forest Products Laboratory, One Gifford Pinchot Drive, Madison, WI 53726, USA
e-mail: jjakes@fs.fed.us

S. V. Pingali · S. Qian · W. T. Heller
Biology and Soft Matter Division, Oak Ridge National Laboratory, 1 Bethel Valley Road, Oak Ridge, TN 37831, USA

Introduction

Lignocellulosic materials from agriculture and forest biomass are becoming an increasingly important component of our sustainable future. Recently, much research effort has focused on sustainably producing fuels (Nanda et al. 2014) and industrial chemicals (Sheldon 2014) from lignocellulosic materials. New nanomaterials, such as cellulose nanocrystals (Moon

et al. 2011) and lignin-based carbon nanofibers (Lai et al. 2014), are being developed for high-performance materials. However, not to be overlooked is the role of forest products in the sustainability of our building materials and the need for continued research to elucidate molecular-scale phenomena that lead to improved durability and the development of new products. Traditional forest products, including solid dimensional lumber, plywood, oriented strandboard, fiberboard, and laminated veneer lumber, continue to be the most cost-effective construction materials of choice for many applications. New advanced forest products, such as cross-laminated timber, are being developed and becoming viable substitutes for steel and concrete in larger structures, such as mid-rise buildings and bridges (Robertson et al. 2012; Lehmann 2013). From an environmental perspective, forest products are attractive because wood not only can be sustainably sourced, but also results in less air and water pollution than concrete and steel (Lippke et al. 2004; Bergman et al. 2014; Oliver et al. 2014).

An improved understanding of wood structure and moisture sorption effects across all length scales is needed to accelerate the development of forest products with improved durability, including dimensional stability and resistance to fungal decay. Small angle neutron scattering (SANS) is well-suited to study wood nanostructure, which is necessary to connect molecular-scale phenomena to bulk properties. However, the complex wood structure results in complicated scattering patterns that can be difficult to interpret. Basic softwood structure is shown in Fig. 1. Growth rings in the tree stem define the tangential-longitudinal, radial-longitudinal, and transverse primary planes in wood (Fig. 1a). Each growth ring has earlywood and latewood rings, which have thin and thick cell walls, respectively (Fig. 1b). More than 90 % of cells are longitudinal tracheids, although there are also a few ray cells oriented perpendicular to the growth rings in the transverse plane (Fig. 1b; Wiedenhoef 2013). Pits facilitate liquid transport between cells. Tracheid walls are made of a primary and three secondary cell wall layers (S1, S2, and S3), and neighboring cells are held together by the lignin-rich middle lamella (Fig. 1c). Secondary cell walls consist of parallel cellulose microfibrils helically embedded in a matrix of lignin and hemicelluloses. The angle the cellulose microfibrils make with the longitudinal tracheid axis is called the microfibril

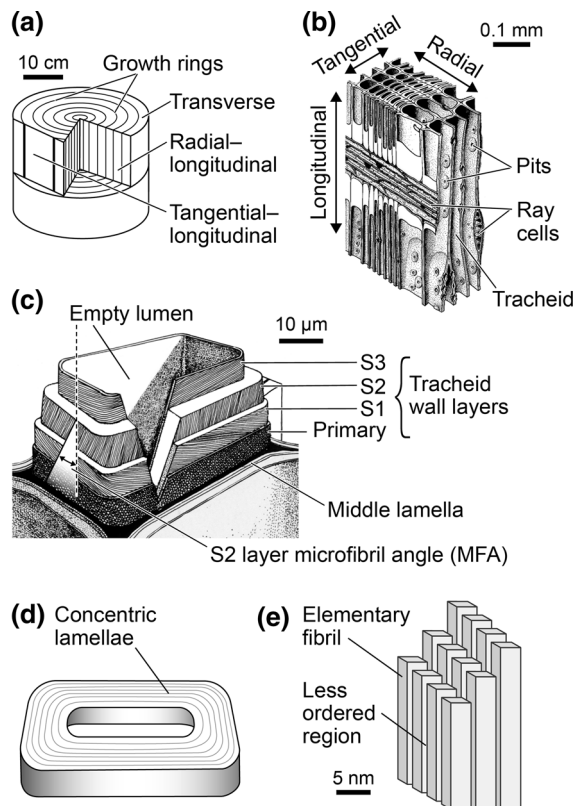


Fig. 1 Breakdown of hierarchical softwood structure illustrating the **a** bulk, **b** cellular, **c** tracheid wall layers, **d** S2 tracheid wall layer, **e** microfibril levels

angle (MFA). The thickest and most dominant layer is the S2; and its MFA, typically between 5° and 30° , is fairly constant within the tracheids in a growth ring. In the S1 and S3 layers, the MFA is much higher, typically 50° – 70° and $>70^\circ$, respectively, and can vary substantially within a given layer (Wiedenhoef 2013). Although the detailed structure of the S2 is still debated, most evidence suggests that in the transverse plane the microfibrils are organized in concentric lamellae (Fig. 1d) that have 15–25 nm thickness corresponding to the approximate diameter of a cellulose microfibril (Fahlén and Salmén 2002; Salmén and Fahlén 2006). Cellulose microfibrils are composed of semicrystalline elementary fibrils, which are approximately 3 nm across (Jakob et al. 1996) and have less ordered regions between them (Fig. 1e). The elementary fibril cross section is likely composed of 18 or 24 semicrystalline cellulose chains (Fernandes et al. 2011; Newman et al. 2013; Thomas et al. 2013).

The moisture content (MC) in wood, defined as water mass divided by oven-dried wood mass, depends on temperature and relative humidity (RH). Water is absorbed by the accessible hydroxyl and other polar chemical groups in the amorphous cellulose, hemicelluloses, and lignin. Recent molecular dynamics simulations studying water sorption in amorphous cellulose and hemicelluloses provide new insights and suggest that at MCs below 10 %, water is initially bound in the empty spaces between the amorphous polymers, resulting in minimal swelling, whereas at higher MCs, each additional water molecule increases the volume equally and swelling is directly proportional to MC (Kulasinski et al. 2014, 2015a, c). At the fiber saturation point (FSP), which depending on definition is between 30 and 40 % MC, (Stamm 1971; Hernández and Bizoň 1994; Berry and Roderick 2005; Englund et al. 2013) the maximum capacity for bound water is reached, and at higher MCs free water forms in wood cavities. What is not understood is how molecular-scale water sorption and swelling relate to swelling throughout wood's hierarchical structure and bulk wood properties.

In recent years, SANS has become an increasingly popular tool in lignocellulosic research, particularly to study the effects of pretreatments on the morphology and nanostructure of various types of biomass (Pingali et al. 2010, 2014; Nishiyama et al. 2014). Nevertheless, SANS has not yet been utilized to study the combined effect of anisotropy and moisture-induced swelling in wood nanostructure or as an operative tool for forest products research. In this work, we studied anisotropic structure and moisture-induced swelling in loblolly pine as a function of RH over a broad range of length scales (1–600 nm). Detailed information about elementary fibril swelling was gained, and it was shown that over half the transverse swelling in the S2 cell wall layer derives from swelling between elementary fibrils in the cellulose microfibrils. Swollen regions between elementary fibrils may also be the hypothesized diffusion channels that are responsible for onset of fungal decay (Jakes et al. 2013). In addition, 25- μm -thick longitudinal sections were studied to mimic the swelling behavior of cut wood cell walls near wood-adhesive bondlines, and it was found that the elementary fibrils in cut wood cell walls swell more than in intact cells above 90 % RH. The broad implications for strategies to improve forest products and how to use SANS in forest products research are also discussed.

Experimental procedure

Specimen preparation

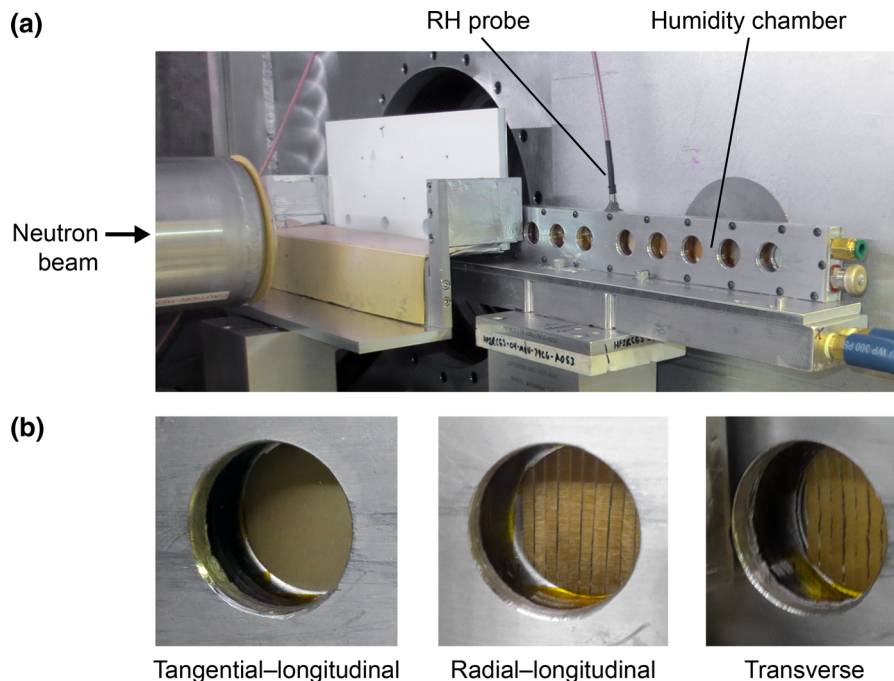
Latewood sections (0.5 mm thick) of each primary orientation (transverse, radial-longitudinal, and tangential-longitudinal) were prepared for SANS from a single growth ring of loblolly pine (*Pinus taeda*) using a razor blade guillotine. Additionally, 25- μm -thick tangential-longitudinal and radial-longitudinal sections were prepared using a sled microtome equipped with disposable microtome blades. A stack of 20 thin sections was used to replicate the scattering path length of the 0.5-mm-thick intact specimens. Samples were secured using polyamide tape between two square Al holders (25 mm²) with 19-mm circular holes. When the transverse sections were wetted and secured at both ends, they bowed out of plane because of moisture-induced swelling. To prevent bowing, only one end was secured while the other was allowed to swell freely. Because latewood bands are only a few millimeters thick, multiple transverse and radial-longitudinal sections were placed next to each other to fill the area illuminated by the beam. All specimens were soaked in D₂O (99.8 % atom % D, Sigma-Aldrich) for 24 h to improve signal-to-noise ratio by exchanging the hydroxyl groups in the water-accessible wood polymers to deuterioxyl groups, (Fernandes et al. 2011; Nishiyama et al. 2014) which decreased their incoherent scattering.

Humidity chamber

An RH chamber, custom-built from aluminum with circular quartz windows (Fig. 2a), was used to test the samples conditioned at humidity ranging from 25 to 95 % in situ. Samples immersed in D₂O (100 % RH) were also tested using square quartz liquid cells. Samples secured inside the Al holders were mounted inside the RH chamber onto the windows nearest to the detector, as shown in Fig. 2b. Tangential-longitudinal and radial-longitudinal sections were mounted with the longitudinal direction perpendicular to the neutron beam in the vertical direction. The transverse sections were mounted with the tangential direction perpendicular to the neutron beam in the vertical direction.

The humidity inside the chamber was controlled using an L&C Science and Technology (Hialeah, FL, USA) RH-200 relative humidity generator. D₂O (99.8 % atom % D, Sigma-Aldrich) was used instead

Fig. 2 **a** Custom-built humidity chamber used at the Oak Ridge National Laboratory HFIR Bio-SANS beamline. **b** View of 0.5-mm-thick wood sections secured in the humidity chambers seen through the quartz windows



of H₂O in the RH generator to minimize incoherent scattering from humidified air in the sample chamber. Also by using D₂O, the contrast between the moisture-swollen wood polymers and the water-inaccessible wood polymers was increased. Samples conditioned at different humidity levels were measured at the Bio-SANS instrument (Heller et al. 2014) at the High Flux Isotope Reactor at Oak Ridge National Laboratory (Oak Ridge, TN, USA). After removing the samples from the 24 h D₂O soak they were patted dry and conditioned with dry air inside the humidity chamber for 12 h. Then the samples were conditioned for 3 h at each RH step prior to data collection. Experiments were performed in absorption with increasing RH values of 24, 51, 68, 77, 89, and 96 %. Samples immersed in D₂O were measured at the EQ-SANS instrument (Zhao et al. 2010) at the Spallation Neutron Source at Oak Ridge National Laboratory (Oak Ridge, TN, USA).

Instrument configuration at Bio-SANS

Multiple instrument configurations were used to collect the broadest range of scattering vectors available at the Bio-SANS beamline. To cover the range $0.001 \text{ \AA}^{-1} < q < 0.55 \text{ \AA}^{-1}$, sample-to-detector (SDD) distances of 0.3 and 6 m at wavelength $\lambda = 6 \text{ \AA}$ and 14.5 m at $\lambda = 18 \text{ \AA}$ with a neutron spread $\Delta\lambda/\lambda = 0.15$ were

used. However, the time to collect this full q range was prohibitively long to collect data at many humidity points due to much lower neutron flux at $\lambda = 18 \text{ \AA}$. Therefore, the full q range was collected only at 89 % RH for all 0.5-mm-thick sample orientations and at 45 % RH for the tangential-longitudinal sample. Data were collected at more humidity levels at an additional configuration that covered a shorter q range of $0.007 \text{ \AA}^{-1} < q < 0.55 \text{ \AA}^{-1}$ using a $\lambda = 6 \text{ \AA}$ with a neutron spread $\Delta\lambda/\lambda = 0.15$, and sample to detector distances of 0.3 and 6 m. Circular aperture diameters of 40 and 12 mm for source and sample, respectively, were used for all measurements. A 2D ($1 \times 1 \text{ m}^2$) ³He linear position-sensitive detector made up of 192×256 pixels was used to record the data. Detector images were normalized to the incident beam and monitor counts; corrected for pixel sensitivity, detector dark current, and background contributions; and scaled to absolute units.

Instrument configuration at EQ-SANS

Two different instrument configurations were used to attain a broad range of scattering vectors ($0.004 \text{ \AA}^{-1} < q < 0.55 \text{ \AA}^{-1}$). The lower q range ($0.004 \text{ \AA}^{-1} < q < 0.06 \text{ \AA}^{-1}$) was obtained using an SDD of 4 m and a minimum wavelength $\lambda_{\min} = 9 \text{ \AA}$. The high q range ($0.03 \text{ \AA}^{-1} < q < 0.55 \text{ \AA}^{-1}$) was

obtained using SDD of 1.3 m and $\lambda_{\min} = 2.5 \text{ \AA}$. The beam was collimated using a source aperture of 25 mm and a sample aperture of 12 mm. A 2D ($1 \times 1 \text{ m}^2$) ^3He position-sensitive detector made up of 192×256 pixels was used to record the data. Two-dimensional data were reduced and corrected for dark current, sample transmission, and detector sensitivity using MantidPlot (Arnold et al. 2014).

Anisotropic data reduction

The radial distance from the beam center in the detector images was converted to the reciprocal space wave transfer vector

$$q = \frac{4\pi \sin \theta}{\lambda} \quad (1)$$

where θ is scattering angle and λ is neutron beam wavelength. Then, the 2D SANS data were anisotropically reduced to 1D using the sector averaging routines provided at the Bio-SANS and EQ-SANS beamlines. At Bio-SANS, for the tangential-longitudinal and radial-longitudinal specimens the sector azimuthal averaging was performed using the auto-anisotropy, twofold symmetry tool implemented in an Igor Pro package. Using the tool the intensity for every q value was determined, and then the azimuthal angle range was selected to be within 25 % of maximum intensity for equatorial scattering and within 25 % of minimum intensity for meridional scattering. Scattering outside those sectors was discarded. For the transverse specimens the scattering patterns were asymmetric. Therefore, the sector sizes needed to be set manually and the azimuthal angular ranges adjusted in relation to the asymmetric diffraction peaks as will be illustrated in the results section. At EQ-SANS, data reduction and azimuthal averaging were performed in MantidPlot, with the sector sizes set manually at 20° and the azimuthal angular ranges based on the Bio-SANS analysis.

To further quantify differences between scattering patterns and learn more about the origins of scattering, the reduced data from sectors with strong diffraction peaks were fitted to a model with two power laws and a Gaussian peak:

$$I(q) = B_1 q^{-P_1} + B_2 q^{-P_2} + A e^{-\frac{(q-q_0)^2}{\sigma^2}} + B_3 \quad (2)$$

The variables in Eq. 1 correspond to power law exponents P_1 and P_2 ; scaling factors B_1 , B_2 , and A ; peak position q_0 with peak width σ ; and background B_3 . The fit convergence was based on a nonlinear least squares regression that was implemented in the Irena package (Ilavsky and Jemian 2009). Uncertainty of the parameters was determined by calculating the range of parameter values in which the $\chi_{\text{fit}}^2 < 1.05 \chi_{\text{critical}}^2$.

Results

2D SANS patterns from sections prepared with transverse, radial-longitudinal, and tangential-longitudinal orientations exhibited unique anisotropic scattering over a broad q range (Fig. 3). Relatively small differences were observed in scattering patterns between radial-longitudinal and tangential-longitudinal specimens, whereas large differences were observed between the transverse specimen and the other two.

Anisotropic scattering in the low- q range (Fig. 3a, d, g, j) provided information about large structural features ($54 \text{ nm} < d < 600 \text{ nm}$). In the radial-longitudinal and tangential-longitudinal sections, the longitudinal tracheid axis was oriented perpendicular to the neutron beam in the vertical direction. The pronounced orientational scattering along the equatorial axis in the scattering patterns likely arose from the lamellar structure in the S2 cell wall layer. The more intense equatorial scattering in the radial-longitudinal than the tangential-longitudinal section suggested a more pronounced long range order. Longitudinal tracheids have a nominally rectangular cross section (Fig. 1b), and in the radial-longitudinal orientation the longer side of the rectangle was oriented parallel to the beam; therefore, a larger volume fraction of the concentric lamellae in the S2 cell wall layer (Fig. 1d) were oriented parallel to the beam, which is consistent with the more intense equatorial scattering observed in the radial-longitudinal section. Distinct meridional scattering was also observed in the radial-longitudinal section, but not the tangential-longitudinal section. This meridional scattering likely arose from the ray cells (Fig. 1b). In loblolly pine, these ray cells include ray tracheids (Howard and Manwiller 1969), which similar to the longitudinal tracheids have

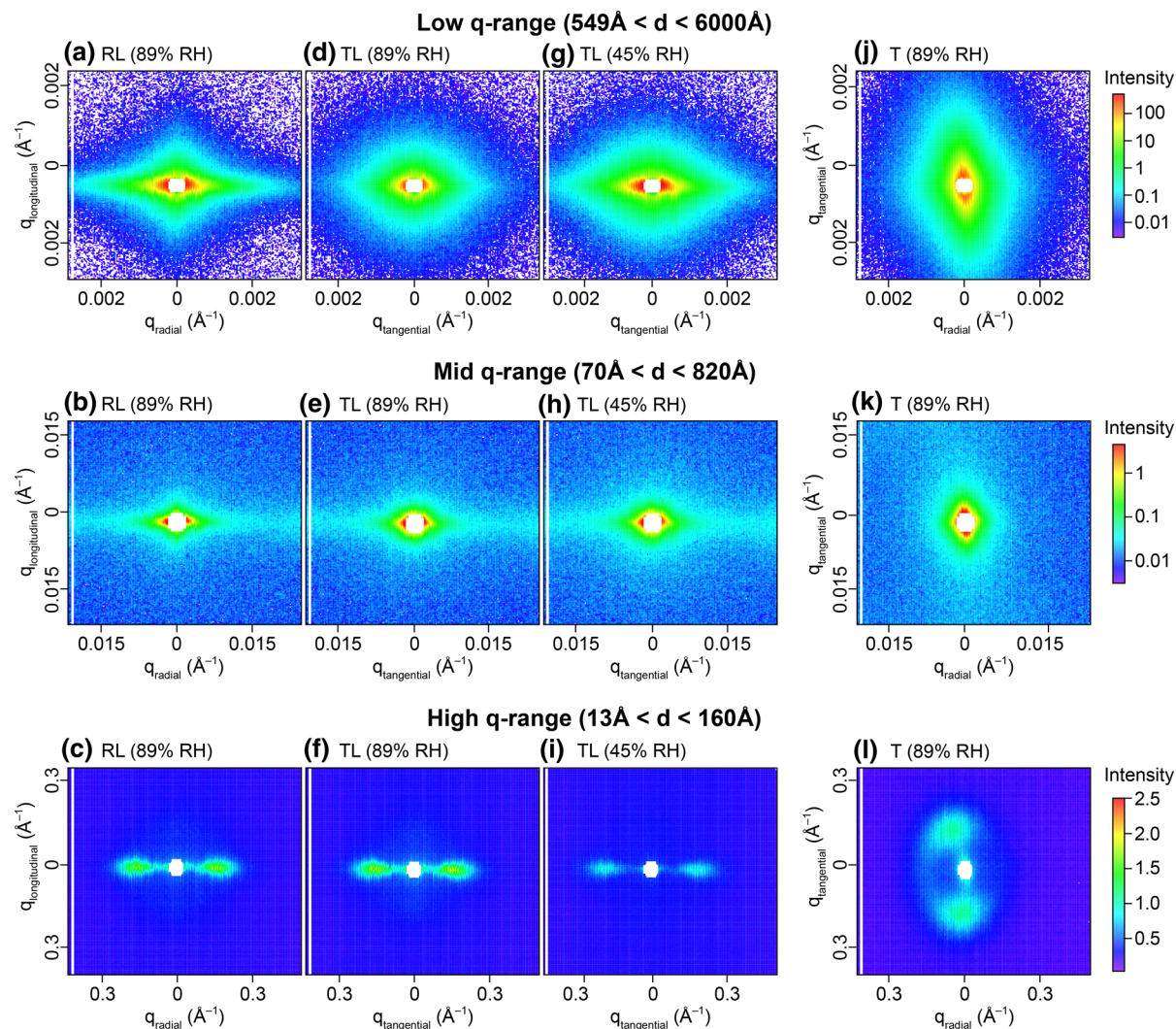


Fig. 3 Two-dimensional anisotropic scattering patterns of 0.5-mm-thick wood sections over a broad q range from each primary orientation: **a–c** radial-longitudinal (RL), **d–i** tangential-longitudinal (TL), and **j–l** transverse (T). Results are from 89 % RH

(**a–f**, **j–l**) and 45 % RH (**g–i**) conditioning. The white spot in the center of detector image is the shadow of the beam stop

secondary cell wall layers with cellulose microfibrils organized in lamellar structures. In radial-longitudinal sections, the ray cells have their long axis oriented perpendicular to the neutron beam in the horizontal direction and their lamellae caused preferential scattering in the meridional direction.

In an ideal transverse section, the longitudinal axis of the tracheids is oriented parallel to the neutron beam. However, using an optical microscope post-experiment, it was found that the longitudinal axis of the tracheids was tilted approximately 16° with respect

to the incident beam during these experiments. The transverse 2D SANS pattern at low q displayed bidirectional scattering enhanced along an axis about 10° from the meridional axis, indicating there was a higher volume fraction of S2 cell wall lamellae oriented parallel to the beam along an axis about 10° from the meridional axis. Similar to the radial-longitudinal section, the transverse section had ray cells with their long axis oriented perpendicular to the neutron beam in the horizontal direction, but meridional scattering from the ray cells was too weak to be observed.

At the mid- q range, scattering from smaller features ($7 \text{ nm} < d < 82 \text{ nm}$) led to anisotropic scattering patterns that were similar in shape to the low- q patterns, suggesting they provide similar structural information (Fig. 3b, e, h, k). Cellulose microfibrils, which are groups of elementary fibrils (Fig. 1e), were expected to scatter at this length scale. However, no structural information could be gained about microfibrils, perhaps because there was not sufficient long range order of microfibrils, the contrast between microfibrils and the surrounding less ordered regions was too weak, or the scattering was convoluted with contributions from other features.

Anisotropic scattering at high- q range (Fig. 3c, f, i, l) provided information about smaller structural features ($1.3 \text{ nm} < d < 16 \text{ nm}$). The patterns were dominated by elementary fibril diffraction peaks arising from the contrast between the D_2O absorbed by the less ordered regions of the cellulose microfibrils and the interiors of the D_2O -inaccessible semicrystalline elementary fibrils (Fig. 1e). Strong equatorial diffraction peaks were observed in the tangential-longitudinal and radial-longitudinal sections, and asymmetric diffraction peaks were observed in the transverse section. The equatorial diffraction peaks have been correlated to the distance between neighboring elementary fibrils (Fernandes et al. 2011; Thomas et al. 2013). The similar equatorial diffraction peaks in the radial-longitudinal and tangential-longitudinal sections showed that at this length scale the scattering is not dependent on radial or tangential orientations. The diffraction peaks in the transverse section were asymmetric because the elementary fibrils were aligned close, but not parallel, with the incident beam. Similar asymmetric patterns have been observed in wide angle X-ray micro diffraction studies of crystalline cellulose in Norwegian spruce cell walls and flax fibers when the cellulose microfibrils were tilted with respect to the incident beam at an angle higher than the Bragg angle but less than 90° (Lichtenegger et al. 1999; Paris and Müller 2003). Meridional diffraction peaks from elementary fibrils embedded in the ray tracheid cell walls were not observed in the radial-longitudinal or transverse sections. This was not unexpected because the scattering intensity is proportional to the square of the scattering volume, which was very small compared to the longitudinal tracheids.

The 2D SANS patterns of stacked 25- μm -thick radial-longitudinal or tangential-longitudinal sections (not shown here) were similar to their corresponding pattern from the intact 0.5-mm sections. The only observable difference was that the equatorial diffraction peak at high q in the tangential-longitudinal stack was more diffuse, suggesting slight misalignment in the stacking of the 25- μm -thick sections.

SANS patterns over a broad q range from a 0.5-mm tangential-longitudinal section held at 89 and 45 % RH are shown in Fig. 3d–f, g–i, respectively, and provided information about how wood nanostructure and the resultant neutron scattering changed with moisture content. At low q , equatorial scattering becomes less intense with increasing RH, indicating less contrast between the scattering features. The features dominating scattering at these length scales were likely the S2 layer lamellae composed of cellulose microfibrils. The D_2O being absorbed within the microfibrils at increasing RH appeared to decrease the lamellae contrast. There were no obvious differences in the mid- q range. The diffraction peak at high q (Fig. 3f, i) shifted towards higher q with decreasing RH, meaning that the spacing between the elementary fibrils decreased. The diffraction peak intensity was also substantially attenuated because the contrast between the elementary fibrils and less ordered regions decreased as D_2O desorbed from the less ordered regions.

Symmetric strong and weak diffraction sectors (Fig. 4a) were used for tangential-longitudinal and radial-longitudinal anisotropic data reductions, whereas asymmetric sectors (Fig. 4b) were used for the transverse data. The reduced data and model fits to the strong diffraction sectors are shown in Fig. 4c. A consistent power law of $\sim q^{-4}$ was observed for all orientations and RH conditions in the lowest q range ($q < 0.01 \text{ \AA}^{-1}$), see line with power law of q^{-4} in Figs. 4c and 5a. According to Porod (Glatter and Kratky 1982) this corresponds to scattering from well-defined interfaces between volumes whose radii of gyration are likely much larger than the q range probed in these experiments. Scattering from the interfaces between the concentric lamellae are the most likely contributors to this surface scattering because compared to other internal surfaces, namely empty wood cavities, they have a higher number density and higher contrast. The constant

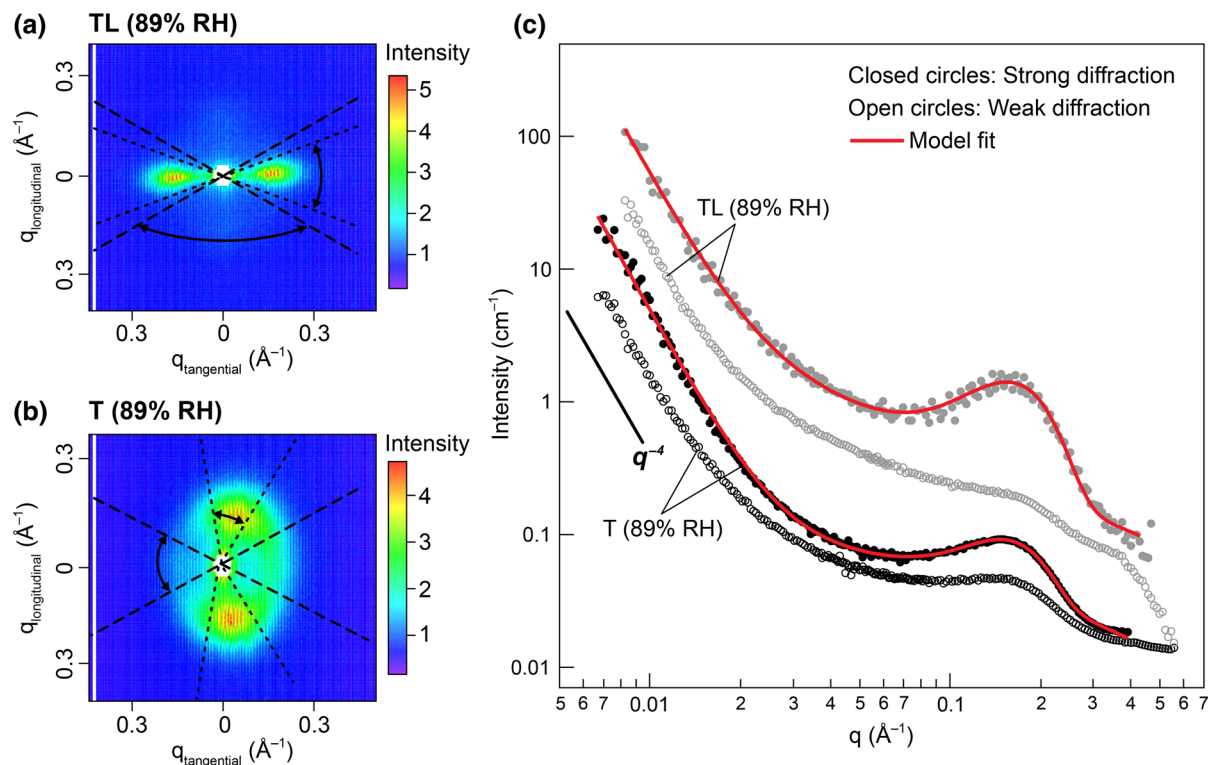


Fig. 4 SANS patterns from **a** a tangential-longitudinal (TL) section and **b** a transverse (T) section held at 89 % RH showing representative strong diffraction sectors (*dotted lines*) and weak diffraction sectors (*dashed lines*) used for anisotropic data reduction. **c** Azimuthally averaged data in absolute units from

the strong diffraction sectors (*closed circles*) and weak diffraction sectors (*open circles*). The fits of the strong diffraction data to the model $I(q)$ in eq. 2 of two power laws and a Gaussian peak are also shown (*red line*)

power law indicated the surface roughness was not moisture dependent and therefore absorbed water is not changing the texture of the lamellar surface. The highest- q power law exponent, P_2 in Eq. 2, corresponded to $\sim q^{-1}$ for the tangential-longitudinal and radial-longitudinal sections above 80 % RH, suggesting for these orientations and moisture levels the form factor scattering was dominated by rods, which could be either the elementary fibrils or the elongated D_2O swollen polymers between the elementary fibrils. In SANS, form factor scattering results from scattering of a “particle” with a given shape and size distributions. However, for the transverse section and the tangential-longitudinal and radial-longitudinal sections below 80 % RH, the scattering was either highly convoluted or extremely weak, which resulted in lower P_2 values. At high q , the reduced data from the strong diffraction sectors possess obvious diffraction peaks. Interestingly, data from the weak diffraction sectors also show

a small peak or shoulder. This feature is likely the cumulative effect of elementary fibrils in domains other than the longitudinal tracheid S2 layers, such as the S1 and S3 layers or the ray cells.

Both the diffraction peaks in the strong diffraction sectors and shoulders in the weak diffraction sectors shifted towards higher q with decreasing RH for all specimens tested, similar to the tangential-longitudinal section 1D reduced data shown in Fig. 5a. This indicated a change in elementary fibril spacing with moisture content. Changes in elementary fibril spacing with moisture content were also observed in previous research using SANS (Fernandes et al. 2011; Thomas et al. 2014) and small angle X-ray scattering (Jakob et al. 1996; Kennedy et al. 2007). The strong diffraction peaks in Fig. 5a were tracked as a function of RH and the peak positions q_0 related to the elementary fibril spacings d using $q_0 = 2\pi/d$. The changes in elementary fibril spacing with RH (Fig. 5b)

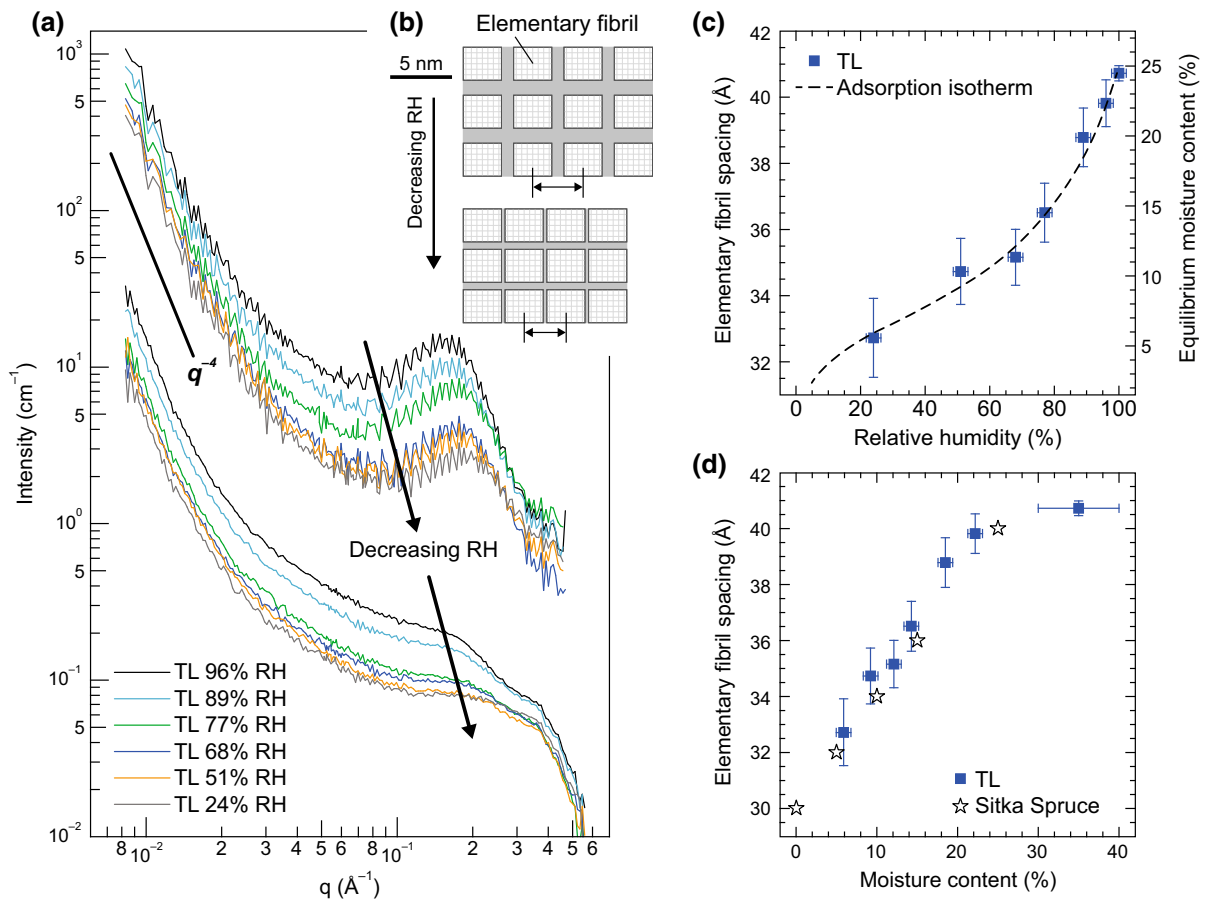


Fig. 5 Swelling of bundles of elementary fibrils. **a** 1D reduced data from tangential-longitudinal (TL) latewood section obtained from 25 to 96 % RH during absorption, showing how both weak and strong diffraction peaks shift towards higher q as **b** the spacing between elementary fibrils in the microfibrils decreased. **c** Plot of the swelling of the elementary fibril spacing as a function of RH, showing the behavior is similar to loblolly pine absorption isotherm (Zelinka and Glass 2010). **d** Plot of the

elementary fibril spacing versus MC, showing our data agrees with values reported on earlywood Sitka spruce (Fernandes et al. 2011). The MC of the RH conditioned specimens was calculated based on the absorption sorption isotherm (c) while the MC of the immersed samples was estimated as 35 % based on the 30–40 % MC range for fiber saturation values reported in the literature (Stamm 1971; Hernández and Bizoñ 1994; Berry and Roderick 2005; Engelund et al. 2013)

follow the same trend as MC of bulk wood (Fig. 5c). Quantitatively, the elementary fibril spacing for the tangential-longitudinal 0.5-mm section agreed with the reported values for earlywood Sitka spruce (Fernandes et al. 2011; Fig. 5d). Additionally, the spacing increases linearly with MC between 10 and 25 % MC as supported by molecular dynamic simulations (Kulasinski et al. 2015a). However, the elementary fibril spacing behavior seems to change at the highest MCs. By definition, the amount of absorbed water in the wood cell walls immersed in water should be the same as at fiber saturation point. Therefore, the MC of the immersed specimen can be estimated as the fiber

saturation point MC and in Fig. 5d is plotted in the 30–40 % MC range (Stamm 1971; Hernández and Bizoñ 1994; Berry and Roderick 2005; Engelund et al. 2013). The spacing between the elementary fibril appears to either reach a maximum below fiber saturation point at approximately 25 % MC or be no longer proportional to MC at the highest MCs.

The same elementary fibril spacing was measured from each of the three primary orientations (Fig. 6a), demonstrating that the transverse section diffraction peaks are also arising from elementary fibril spacing and any wood orientation could be used to accurately measure elementary fibril spacing. The elementary

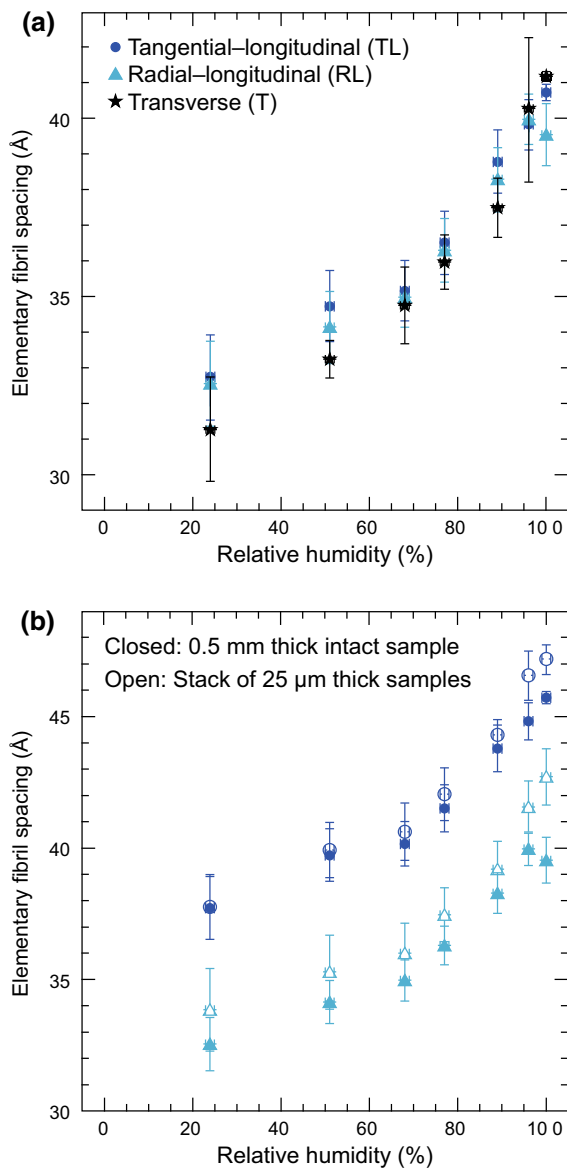


Fig. 6 Trends in the swelling of the elementary fibril spacing. **a** No difference is evident between the three primary orientations, namely, tangential-longitudinal, radial-longitudinal, and transverse. **b** At high RH, the stacks of 25- μ m-thick sections exhibited higher elementary fibril spacings. Tangential-longitudinal (TL) data curves have been offset by 5 Å from the radial-longitudinal (RL) curves for clarity. Samples immersed in D_2O are plotted at 100 % RH

fibril spacings of stacks of 25- μ m-thick samples and 0.5-mm-thick intact samples are compared in Fig. 6b. The elementary fibril spacing was similar between the stack of 25- μ m-thick sections and the intact specimen except at the RH above 90 % and under D_2O

immersion, in which the stacks had higher spacing. This suggests that swelling between the elementary fibrils of cut cells, such as in wood-adhesive bondlines, are only different at the highest moisture contents.

Discussion

Results from wood sections cut from the three primary orientations (Fig. 3) show that it is possible to gain insight into the three-dimensional nanostructural features within the cell wall from the three-dimensional reciprocal space by testing different orientations. However, these results also demonstrate that when using small angle scattering as a tool in lignocellulosic biomass research, such as biorefinery pretreatments, (Nishiyama et al. 2014) or in future forest products research, the orientation and moisture content of the wood section must be carefully controlled for optimal results. Cell wall lamellar scattering likely dominated the low- q scattering and is orientation and moisture dependent, with the most pronounced scattering from the radial-longitudinal orientation and in the middle ranges of RH. Additional experiments, such as rocking curve experiments, are needed to further understand the sensitivity to slight misorientations between the wood primary planes and neutron beam on the scattering patterns. However, obtaining quantitative information about the elementary fibril spacing in the high- q range is not orientation dependent.

Swelling and shrinking of wood caused by changes in moisture content is one of the major durability issues in forest products. An improved understanding of the underlying swelling processes would accelerate the development of both bulk wood chemical modifications to improve dimensional stability and moisture durable wood adhesives. It is generally accepted that the stiff cellulose microfibrils, which are for the most part aligned longitudinally in wood, restrict swelling strains in that direction to <0.1 %. However, swelling strains in the transverse plane are much higher and depend on the structural level at which they are measured. In Fig. 7, transverse swelling strains as a function of humidity conditioning at the cellular, S2 tracheid wall layer, and microfibril levels are plotted. All the strains are from latewood in a softwood species. Transverse isotropy is observed in swelling strains at the cellular and microfibril length scales,

Microfibril level (this work)

- Tangential longitudinal section
- ▲ Radial longitudinal section

S2 Tracheid wall level (Rafsanjani et al. 2014)

- Tangential side wall, normal to the wall thickness
- ☆ Tangential side wall, parallel to the cell wall thickness
- △ Radial side wall, normal to the cell wall thickness
- ◇ Radial side wall, parallel to the cell wall thickness

Latewood cellular level (Derome et al. 2011)

- + Tangential longitudinal direction
- × Radial longitudinal direction

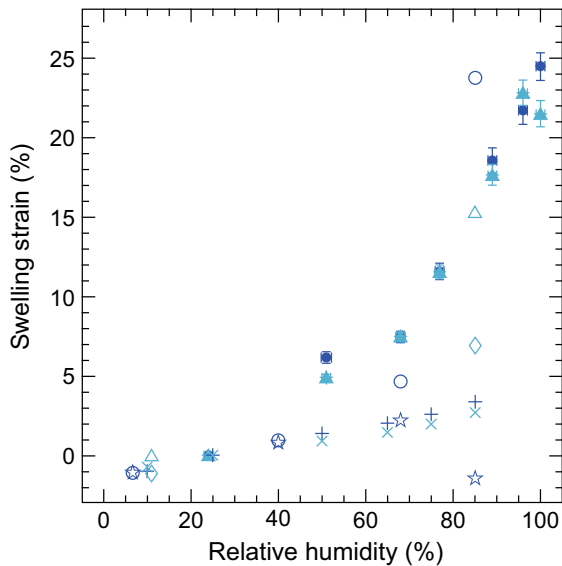


Fig. 7 Moisture-induced strain in wood at the cellular (Derome et al. 2011), S2 cell wall (Rafsanjani et al. 2014), and microfibril levels (this work)

whereas anisotropic swelling occurs in the secondary cell wall. Strains are about an order of magnitude higher in the microfibrils than at the cellular scale, suggesting the structure of wood connecting these length scales accommodates a large portion of the strain. In the S2 secondary cell wall, the plotted strains are much higher in the direction normal to the cell wall thickness than parallel to the cell wall thickness, (Rafsanjani et al. 2014) which is in agreement with other work (Ishimaru and Iida 2001; Murata and Masuda 2006).

Previous researchers proposed that the majority of moisture is absorbed between the concentric microfibril lamellae in the secondary cell walls and that is why the S2 tracheid wall layer swelling is greatest in the direction normal to cell wall thickness (Bouteje 1962;

Rafsanjani et al. 2014). However, simple calculations based on the data in Fig. 7 show that in the transverse plane the contributions of microfibril swelling in the S2 secondary cell wall layer are greater than the total sum of the remaining components. In Fig. 7, strains are set to 0 at 25 % RH and results are available for both the S2 secondary cell wall and elementary fibrils from 25 to 85 % RH. Over this range, the S2 secondary cell wall swells about 20 and 4 % in the directions perpendicular and parallel to the cell wall thickness, respectively, resulting in an overall 25 % increase in transverse plane area. For elementary fibrils over the same humidity range, an approximately 16 % strain increase is observed and, assuming a rectangular microfibril cross section, results in a 35 % increase in microfibril cross-section area. Now, considering that cellulose microfibrils account for about 40 % of the area in the S2 secondary cell wall transverse plane, (Rowell et al. 2005) about 55 % of the S2 secondary cell wall swelling in the transverse plane originates in the microfibril. Hence, chemical modifications and adhesives must target and prevent swelling in the microfibrils to improve moisture-related dimensional stability in forest products.

Anisotropic swelling in the transverse plane of the S2 secondary cell wall likely arises from structural features within and between the concentric microfibril lamellae, and not anisotropic transverse swelling of the microfibrils themselves. It is conceivable that a microfibril with regularly oriented elementary fibrils swells anisotropically because different surfaces of cellulose crystals have different degrees of hydrophilicity that would absorb water differently (Bondeson et al. 2006). Then, if the microfibrils were regularly oriented in the concentric lamellae, anisotropic swelling in the microfibrils could contribute to anisotropic swelling of the concentric lamellae and the S2 secondary cell wall. However, it is unlikely such regular ordering of the elementary and microfibrils exists. Both experimental and theoretical results showed a longitudinal twist in both elementary fibrils and microfibrils, (Hanley et al. 1997; Bondeson et al. 2006; Atalla et al. 2014) which would average out any potential anisotropic microfibril swelling contributions to the S2 secondary cell wall anisotropic swelling.

Before adhesive application in modern forest products, such as plywood, laminated veneer lumber, and cross-laminated timber, wood surfaces are

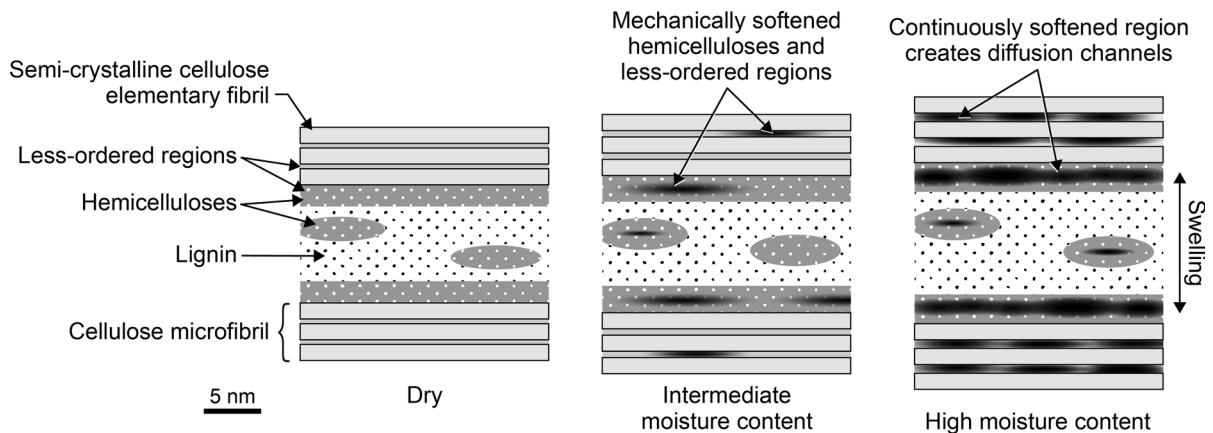


Fig. 8 Refined schematic of the proposed creation of diffusion channels during moisture uptake in the S2 cell wall layer nanostructure

typically cut with sharp blades either in a planer or veneer cutting process (Frihart 2005). The result is often a longitudinally cut wood cell at the interface between the adhesive and wood substrate in the bondline. The stacks of 25- μm -thick sections studied were meant to mimic those cut cells and investigate the potential role of the S1 and S3 layers in constraining microfibril swelling. Because the cellulose microfibrils in the S1 and S3 layers are embedded at high ($>50^\circ$) microfibril angles, these layers can withstand large hoop stresses during swelling, which is likely important because compressive swelling stresses up to 90 MPa have been estimated to evolve in wood cell walls during moisture-induced swelling (Tarkow and Turner 1958). Such compressive stresses would be expected to decrease the MC in wood polymers compared to the unstressed state (Kulasinski et al. 2015b). A significant increase in elementary fibril spacing in the cells with cut S1 and S3 layers was only observed at the highest humidity and under D_2O immersion (Fig. 6b). This means that the S1 and S3 layer constraint becomes important only at high levels of moisture-induced strain; and a 0.5-mm-thick intact wood section should be representative of cut wood cells in the bondlines up to 90 % RH in future SANS studies on the effects of wood adhesive cell wall infiltration on moisture-induced swelling of microfibrils.

The approximate 10- \AA increase in elementary fibril spacing during moisture sorption (Fig. 5d) may indicate the creation of diffusion channels for chemical transport through the microfibrils in wood cell walls. Jakes and coworkers recently proposed that the

mechanism for chemical transport through wood cell walls was the percolation of rubbery regions in hemicelluloses and amorphous cellulose networks and that the creation of these diffusion channels is the underlying mechanism responsible for the onset of fungal decay and fastener corrosion in forest products (Jakes et al. 2013). However, in the original schematic, diffusion channels within the microfibrils were not considered. These SANS results informed a refinement to their schematic to include the creation of microfibril diffusion channels. In the new schematic shown in Fig. 8, microfibrils composed of elementary fibrils are at the top and bottom. Disordered cellulose chains, and possibly the hemicellulose glucomannan, (Salmén and Fahlén 2006) compose the disordered regions between elementary fibrils. Amorphous cellulose and hemicelluloses form sheaths around the cellulose microfibrils, (Terashima et al. 2009; Stevanic and Salmén 2009) and hemicelluloses also form networks perpendicular to the cellulose microfibrils (Terashima et al. 2009). The remaining space between microfibrils is filled with lignin. As moisture is absorbed regions of amorphous cellulose and hemicelluloses transform from glassy to mechanically softened rubbery state as they pass through a moisture-induced glass transition, which is expected to occur in approximately the 11–15 % MC range (Cousins 1978; Kelley et al. 1987; Olsson and Salmén 2004). Above a threshold MC, percolated networks of rubbery domains form diffusion channels to facilitate long-range chemical transport. The threshold moisture content for Zn, Cu, K, and Cl ion diffusion in wood cell walls is verified experimentally to be in the same

MC range as the moisture-induced glass transition in hemicelluloses and amorphous cellulose (Zelinka et al. 2015). If the hypothesized connections between elementary fibril swelling, diffusion channel creation, and onset of wood degradation are further confirmed, SANS will be a valuable tool researchers can use to study wood treatments that are known to impart decay resistance, such as current commercial treatments [e.g., acetylation (Rowell et al. 2009)] and heat treatment, and inform both the improvement of these current nontoxic wood protection treatments and the development of future wood protection treatments. Furthermore, these diffusion channels are necessary for the infiltration of chemicals and wood adhesives into the wood nanostructure to improve dimensional stability.

Conclusions

Anisotropic SANS patterns from each primary orientation of wood provided new insights to the three-dimensional nanostructure and moisture-induced swelling in wood. Elementary fibril spacings can be accurately measured from any orientation and increased proportionally with moisture up to approximately 25 % MC, above which the spacing seemed to saturate, suggesting the maximum amount of water absorbed in the microfibril is reached before the bulk wood fiber saturation point. Calculations estimate that swelling between the elementary fibrils accounts for 55 % of the transverse swelling in the S2 cell wall layer; thus, chemical modifications meant to improve moisture-related dimensional stability need to target and prevent the microfibril swelling. Elementary fibril swelling in partially cut cell walls only behaves differently at high MC. Based on the SANS results, we propose that diffusion channels are being created inside microfibrils during moisture sorption. Using established protocols, SANS is now a valuable tool for forest products research that can be used to develop improved wood protection treatments and wood adhesives.

Acknowledgments NP acknowledges the GERS program at UW–Madison, 2012 NSF GFRP and US Forest Service Pathways program for support. JEJ acknowledge funding from 2011 USDA PECASE awards. JEJ and NP acknowledge support from the FHA Cooperative Research Program for Covered Timber Bridges. The use of ORNL High Flux Isotope Reactor

and Spallation Neutron Source was supported by the Scientific User Facilities Division, Office of Basic Energy Sciences, US Department of Energy. SVP acknowledges the Genomic Science Program, Office of Biological and Environmental Research, US Department of Energy (FWP ERKP752). The Center for Structural Molecular Biology operates the Bio-SANS instrument by support from the Office of Biological and Environmental Research (FWP ERKP291), and its facilities are supported by the Office of Basic Energy Sciences, US Department of Energy and managed by UT-Battelle, LLC under contract no. DE-AC05-00OR22725.

References

- Arnold O, Bilheux JC, Borreguero JM et al (2014) Mantid—data analysis and visualization package for neutron scattering and μ SR experiments. Nucl Instrum Methods Phys Res Sect A Accel Spectrometers, Detect Assoc Equip 764:156–166. doi:[10.1016/j.nima.2014.07.029](https://doi.org/10.1016/j.nima.2014.07.029)
- Atalla RS, Crowley MF, Himmel ME, Atalla RH (2014) Irreversible transformations of native celluloses, upon exposure to elevated temperatures. Carbohydr Polym 100:2–8. doi:[10.1016/j.carbpol.2013.06.007](https://doi.org/10.1016/j.carbpol.2013.06.007)
- Bergman R, Puettmann M, Taylor A, Skog KE (2014) The carbon impacts of wood products. For Prod J 64:220–231. doi:[10.13073/FPJ-D-14-00047](https://doi.org/10.13073/FPJ-D-14-00047)
- Berry SL, Roderick ML (2005) Plant-water relations and the fibre saturation point. New Phytol 168:25–37. doi:[10.1111/j.1469-8137.2005.01528.x](https://doi.org/10.1111/j.1469-8137.2005.01528.x)
- Bondeson D, Mathew A, Oksman K (2006) Optimization of the isolation of nanocrystals from microcrystalline cellulose by acid hydrolysis. Cellulose 13:171–180. doi:[10.1007/s10570-006-9061-4](https://doi.org/10.1007/s10570-006-9061-4)
- Bouteje JB (1962) The relationship of structure to transverse anisotropy in wood with reference to shrinkage and elasticity. Holzforschung 16:33–46
- Cousins WJ (1978) Young's modulus of hemicellulose as related to moisture-content. Wood Sci Technol 12:161–167
- Derome D, Griffa M, Koebel M, Carmeliet J (2011) Hysteretic swelling of wood at cellular scale probed by phase-contrast X-ray tomography. J Struct Biol 173:180–190. doi:[10.1016/j.jsb.2010.08.011](https://doi.org/10.1016/j.jsb.2010.08.011)
- Engelund ET, Thygesen LG, Svensson S, Hill CA (2013) A critical discussion of the physics of wood-water interactions. Wood Sci Technol 47:141–161. doi:[10.1007/s00226-012-0514-7](https://doi.org/10.1007/s00226-012-0514-7)
- Fahlén J, Salmén L (2002) On the lamellar structure of the tracheid cell wall. Plant Biol 4:339–345. doi:[10.1055/s-2002-32341](https://doi.org/10.1055/s-2002-32341)
- Fernandes AN, Thomas LH, Altaner CM et al (2011) Nanostructure of cellulose microfibrils in spruce wood. Proc Natl Acad Sci 108:E1195–E1203. doi:[10.1073/pnas.1108942108](https://doi.org/10.1073/pnas.1108942108)
- Frihart C (2005) Adhesive bonding and performance testing of bonded wood products. J ASTM Int 2:12952. doi:[10.1520/JAI12952](https://doi.org/10.1520/JAI12952)
- Glatter O, Kratky O (1982) Small angle X-ray scattering. Academic Press, London
- Hanley S, Revol J-F, Godbout L, Gray D (1997) Atomic force microscopy and transmission electron microscopy of

- cellulose from *Micrasterias denticulata*; evidence for a chiral helical microfibril twist. *Cellulose* 4:209–220. doi:[10.1023/A:1018483722417](https://doi.org/10.1023/A:1018483722417)
- Heller WT, Urban VS, Lynn GW et al (2014) The Bio-SANS instrument at the high flux isotope reactor of Oak Ridge National Laboratory. *J Appl Crystallogr* 47:1238–1246. doi:[10.1107/S1600576714011285](https://doi.org/10.1107/S1600576714011285)
- Hernández RE, Bizoñ M (1994) Changes in shrinkage and tangential compression strength of sugar maple below and above the fiber saturation point. *Wood Fiber Sci* 26:360–369
- Howard ET, Manwiller FG (1969) Anatomical characteristics of southern pine stemwood. *Wood Sci* 2:77–86
- Ilavsky J, Jemian PR (2009) Irena: tool suite for modeling and analysis of small-angle scattering. *J Appl Crystallogr* 42:347–353. doi:[10.1107/S0021889809002222](https://doi.org/10.1107/S0021889809002222)
- Ishimaru Y, Iida I (2001) Transverse swelling behavior of hinoki (*Chamaecyparis obtusa*) revealed by the replica method. *J Wood Sci* 47:178–184. doi:[10.1007/BF01171219](https://doi.org/10.1007/BF01171219)
- Jakes JE, Plaza N, Stone DS et al (2013) Mechanism of transport through wood cell wall polymers. *J For Prod Ind* 2:10–13
- Jakob HF, Tschegg SE, Fratzl P (1996) Hydration dependence of the wood-cell wall structure in *Picea abies*. A small-angle X-ray scattering study. *Macromolecules* 29:8435–8440. doi:[10.1021/ma9605661](https://doi.org/10.1021/ma9605661)
- Kelley SS, Rials TG, Glasser WG (1987) Relaxation behaviour of the amorphous components of wood. *J Mater Sci* 22:617–624. doi:[10.1007/BF01160778](https://doi.org/10.1007/BF01160778)
- Kennedy CJ, Šturcová A, Jarvis MC, Wess TJ (2007) Hydration effects on spacing of primary-wall cellulose microfibrils: a small angle X-ray scattering study. *Cellulose* 14:401–408. doi:[10.1007/s10570-007-9129-9](https://doi.org/10.1007/s10570-007-9129-9)
- Kulasinski K, Keten S, Churakov SV et al (2014) Molecular mechanism of moisture-induced transition in amorphous cellulose. *ACS Macro Lett* 3:1037–1040. doi:[10.1021/mz500528m](https://doi.org/10.1021/mz500528m)
- Kulasinski K, Guyer R, Derome D, Carmeliet J (2015a) Water adsorption in wood microfibril-hemicellulose system: role of the crystalline-amorphous interface. *Biomacromolecules* 16:2972–2978. doi:[10.1021/acs.biomac.5b00878](https://doi.org/10.1021/acs.biomac.5b00878)
- Kulasinski K, Guyer R, Derome D, Carmeliet J (2015b) Poroelastic model for adsorption-induced deformation of biopolymers obtained from molecular simulations. *Phys Rev E* 92:022605. doi:[10.1103/PhysRevE.92.022605](https://doi.org/10.1103/PhysRevE.92.022605)
- Kulasinski K, Guyer R, Keten S et al (2015c) Impact of moisture adsorption on structure and physical properties of amorphous biopolymers. *Macromolecules* 48:2793–2800. doi:[10.1021/acs.macromol.5b00248](https://doi.org/10.1021/acs.macromol.5b00248)
- Lai C, Zhou Z, Zhang L et al (2014) Free-standing and mechanically flexible mats consisting of electrospun carbon nanofibers made from a natural product of alkali lignin as binder-free electrodes for high-performance supercapacitors. *J Power Sources* 247:134–141. doi:[10.1016/j.jpowsour.2013.08.082](https://doi.org/10.1016/j.jpowsour.2013.08.082)
- Lehmann S (2013) Low carbon construction systems using prefabricated engineered solid wood panels for urban infill to significantly reduce greenhouse gas emissions. *Sustain Cities Soc* 6:57–67. doi:[10.1016/j.scs.2012.08.004](https://doi.org/10.1016/j.scs.2012.08.004)
- Lichtenegger H, Müller M, Paris O et al (1999) Imaging of the helical arrangement of cellulose fibrils in wood by synchrotron X-ray microdiffraction. *J Appl Crystallogr* 32:1127–1133
- Lippke B, Wilson J, Perez-Garcia J et al (2004) CORRIM: life-cycle environmental performance of renewable building materials. *For Prod J* 54:8–19
- Moon RJ, Martini A, Nairn J et al (2011) Cellulose nanomaterials review: structure, properties and nanocomposites. *Chem Soc Rev* 40:3941–3994. doi:[10.1039/c0cs00108b](https://doi.org/10.1039/c0cs00108b)
- Murata K, Masuda M (2006) Microscopic observation of transverse swelling of latewood tracheid: effect of macroscopic/mesoscopic structure. *J Wood Sci* 52:283–289. doi:[10.1007/s10086-005-0760-5](https://doi.org/10.1007/s10086-005-0760-5)
- Nanda S, Mohammad J, Reddy SN et al (2014) Pathways of lignocellulosic biomass conversion to renewable fuels. *Biomass Convers Biorefinery* 4:157–191. doi:[10.1007/s13399-013-0097-z](https://doi.org/10.1007/s13399-013-0097-z)
- Newman RH, Hill SJ, Harris PJ (2013) Wide-angle X-ray scattering and solid-state nuclear magnetic resonance data combined to test models for cellulose microfibrils in mung bean cell walls. *Plant Physiol* 163:1558–1567. doi:[10.1104/pp.113.228262](https://doi.org/10.1104/pp.113.228262)
- Nishiyama Y, Langan P, O'Neill H et al (2014) Structural coarsening of aspen wood by hydrothermal pretreatment monitored by small- and wide-angle scattering of X-rays and neutrons on oriented specimens. *Cellulose* 21:1015–1024. doi:[10.1007/s10570-013-0069-2](https://doi.org/10.1007/s10570-013-0069-2)
- Oliver CD, Nassar NT, Lippke BR, McCarter JB (2014) Carbon, fossil fuel, and biodiversity mitigation with wood and forests. *J Sustain For* 33:248–275. doi:[10.1080/10549811.2013.839386](https://doi.org/10.1080/10549811.2013.839386)
- Olsson AM, Salmén L (2004) The association of water to cellulose and hemicellulose in paper examined by FTIR spectroscopy. *Carbohydr Res* 339:813–818. doi:[10.1016/j.carres.2004.01.005](https://doi.org/10.1016/j.carres.2004.01.005)
- Paris O, Müller M (2003) Scanning X-ray microdiffraction of complex materials: diffraction geometry considerations. *Nucl Instruments Methods Phys Res Sect B Beam Interact Mater Atoms* 200:390–396. doi:[10.1016/S0168-583X\(02\)01728-7](https://doi.org/10.1016/S0168-583X(02)01728-7)
- Pingali SV, Urban VS, Heller WT et al (2010) SANS study of cellulose extracted from switchgrass. *Acta Crystallogr Sect D Biol Crystallogr* 66:1189–1193. doi:[10.1107/S0907444910020408](https://doi.org/10.1107/S0907444910020408)
- Pingali SV, O'Neill HM, Nishiyama Y et al (2014) Morphological changes in the cellulose and lignin components of biomass occur at different stages during steam pretreatment. *Cellulose* 21:873–878. doi:[10.1007/s10570-013-0162-6](https://doi.org/10.1007/s10570-013-0162-6)
- Rafsanjani A, Stiefel M, Jefimovs K et al (2014) Hygroscopic swelling and shrinkage of latewood cell wall micropillars reveal ultrastructural anisotropy. *J R Soc Interface* 11:20140126. doi:[10.1098/rsif.2014.0126](https://doi.org/10.1098/rsif.2014.0126)
- Robertson AB, Lame FCF, Cole RJ (2012) A comparative cradle-to-gate life cycle assessment of mid-rise office building construction alternatives: laminated timber or reinforced concrete. *Buildings* 2:245–270
- Rowell RM, Pettersen R, Tshabalala MA (2005) Cell wall chemistry. In: Rowell RM (ed) *Handbook of wood chemistry and wood composites*, 2nd edn. CRC Press, Boca Raton, pp 33–72

- Rowell RM, Ibach RE, McSweeney J, Nilsson T (2009) Understanding decay resistance, dimensional stability and strength changes in heat-treated and acetylated wood. *Wood Mater Sci Eng* 4:14–22. doi:[10.1080/17480270903261339](https://doi.org/10.1080/17480270903261339)
- Salmén L, Fahlén J (2006) Reflections on the ultrastructure of softwood fibers. *Cellul Chem Technol* 40:181–185
- Sheldon RA (2014) Green and sustainable manufacture of chemicals from biomass: state of the art. *Green Chem* 16:950–963. doi:[10.1039/C3GC41935E](https://doi.org/10.1039/C3GC41935E)
- Stamm AJ (1971) Review of nine methods for determining the fiber saturation point of wood and wood products. *Wood Sci* 4:114–128
- Stevanic JS, Salmén L (2009) Orientation of the wood polymers in the cell wall of spruce wood fibres. *Holzforschung* 63:497–503. doi:[10.1515/HF.2009.094](https://doi.org/10.1515/HF.2009.094)
- Tarkow H, Turner HD (1958) The swelling pressure of wood. *For Prod J* 8:193–196
- Terashima N, Kitano K, Kojima M et al (2009) Nanostructural assembly of cellulose, hemicellulose, and lignin in the middle layer of secondary wall of ginkgo tracheid. *J Wood Sci* 55:409–416. doi:[10.1007/s10086-009-1049-x](https://doi.org/10.1007/s10086-009-1049-x)
- Thomas LH, Altaner CM, Jarvis MC (2013) Identifying multiple forms of lateral disorder in cellulose fibres. *J Appl Crystallogr* 46:972–979. doi:[10.1107/S002188981301056X](https://doi.org/10.1107/S002188981301056X)
- Thomas LH, Forsyth VT, Martel A et al (2014) Structure and spacing of cellulose microfibrils in woody cell walls of dicots. *Cellulose* 21:3887–3895. doi:[10.1007/s10570-014-0431-z](https://doi.org/10.1007/s10570-014-0431-z)
- Wiedenhoeft AC (2013) Structure and function of wood. In: Rowell RM (ed) *Handbook of wood chemistry and wood composites*, 2nd edn. CRC Press, Boca Raton, pp 9–32
- Zelinka SL, Glass SV (2010) Water vapor sorption isotherms for southern pine treated with several waterborne preservatives. *J Test Eval* 38:102696. doi:[10.1520/JTE102696](https://doi.org/10.1520/JTE102696)
- Zelinka SL, Gleber S-C, Vogt S et al (2015) The threshold for ion movement in wood cell walls below fiber saturation observed by micro X-ray fluorescence microscopy. *Holz-forschung* 69:441–448. doi:[10.1515/hf-2014-0138](https://doi.org/10.1515/hf-2014-0138)
- Zhao JK, Gao CY, Liu D (2010) The extended Q-range small-angle neutron scattering diffractometer at the SNS. *J Appl Crystallogr* 43:1068–1077. doi:[10.1107/S002188981002217X](https://doi.org/10.1107/S002188981002217X)